A&A manuscript no.
(will be inserted by hand later)

Your thesaurus codes are:
02. (08.14.1; 02.04.1; 02.13.1; 02.18.6; 02.18.7)

ASTRONOMY
AND
ASTROPHYSICS
24.3.1996

Model neutron star atmospheres with low magnetic fields

I. Atmospheres in radiative equilibrium

V. E. Zavlin[1], G. G. Pavlov[2,3] and Yu. A. Shibanov[3]

[1] Max–Planck–Institut für Extraterrestrische Physik, Giessenbachstrasse, D-85740 Garching, Germany
[2] Pennsylvania State University, 525 Davey Lab, PA 16802, USA
[3] Ioffe Institute of Physics and Technology, 194021, St. Petersburg, Russia

Received . . . . 1996; accepted 1996

Abstract. We present a detailed investigation of neutron star atmospheres with low magnetic fields, $B \lesssim 10^8 - 10^{10}$ G, which do not affect opacities and equation of state of the atmospheric matter. We compute the atmospheric structure, emergent spectral fluxes and specific intensities for hydrogen, helium and iron atmospheres in a wide domain of effective temperatures and gravitational accelerations expected for neutron stars. The iron atmospheres are computed with the opacities and equations of state from the OPAL opacity library. We show that the model atmosphere spectra are substantially different from the blackbody spectra. For light element atmospheres, the flux is greater than the blackbody flux, and the spectrum is harder, at high photon energies, whereas at low energies the spectral flux follows the Rayleigh-Jeans law with a (surface) temperature lower than the effective temperature. The spectra of iron atmospheres display prominent spectral features in the soft X-ray range. The emergent specific intensity is anisotropic, with the anisotropy depending on energy. These properties of the atmospheric radiation should be taken into account for the proper interpretation of the thermal component of the neutron star radiation detectable at X-ray through UV energies. In particular, fitting of the thermal component with the blackbody model may result in substantially incorrect parameters of the radiating regions. We discuss an application of our atmosphere models to the nearby millisecond pulsar PSR J0437 − 4715.

Key words: stars: neutron – dense matter – magnetic fields – radiative transfer – radiation mechanisms: thermal

1. Introduction

Thermal radiation from the surfaces of neutron stars (NSs) provides important information about their thermal histories and the properties of the high-density matter in their interiors (Pethick 1992; Tsuruta 1995). The NS thermal-like radiation has been observed recently in the soft X-ray range with *ROSAT* (Ögelman 1995; and references therein) and *EUVE* (e. g., Foster et al. 1996; Halpern et al. 1996) and in the UV-optical range with *HST* (Pavlov et al. 1996). For the proper interpretation of these observations, one should take into account that NSs are not perfect blackbody emitters — properties of their radiation are determined, like in usual stars, by the radiative transfer in their atmospheres, and the emergent spectra can differ substantially from the Planck spectrum, depending on the chemical composition, magnetic field, energy flux and gravity in surface layers (Pavlov et al. 1995, and references therein).

There are at least two factors which make NS atmospheres different from those of normal stars: the immense gravity and huge magnetic fields. The first factor is important for all NSs; it leads to strong compression and non-ideality of the atmospheric matter, which affects considerably equation of state (EOS) and opacity. Even much greater and more complicated effects on the opacity and EOS can be expected from the very high magnetic field which, in particular, makes the NS atmospheres essentially anisotropic.

First NS atmosphere models have been developed by Romani (1987; hereafter R87). He employed (nonmagnetic) opacities from the Los Alamos Opacity Library (LAOL) to calculate atmosphere models and emergent spectra for a few effective temperatures, $5.5 \leq \log T_{\rm eff} \leq 6.5$, and chemical compositions (pure helium, carbon, oxygen, iron, and a mixture of elements with cosmic abundance) and showed that the spectrum could indeed be quite different from the blackbody, especially for the helium models. Further work has been concentrated on NS atmospheres with "typical" (strong) NS magnetic fields, $B = 10^{11} - 10^{13}$ G, which drastically change opacities and EOS (Miller 1992; Shibanov et al. 1992; Shibanov et al. 1993; Ventura et al. 1993; Pavlov et al. 1994; Pavlov et al. 1995; Shibanov & Zavlin 1995; Shibanov et al. 1995a; Zavlin et al. 1995a). These papers (except that of Miller) were devoted to pure hydrogen NS atmospheres because no reliable opacities and EOS had been developed for non-ideal partly ionized gases of heavier elements. It has been demonstrated that the strong magnetic fields not only dramatically affect the emergent spectra, but they also lead to remarkable anisotropy and strong polarization of the NS thermal radiation.

Importance of the magnetic field depends on how large is the electron cyclotron energy, $h\nu_B = heB/m_e c$, in comparison with other characteristic energies. For instance, if we consider a completely ionized (hot) atmosphere, where the main source of opacity is the free-free transitions and/or scattering on electrons, the opacity is not affected by the field for $h\nu_B \ll h\nu$, k_BT (see, e. g., Kaminker et al. 1983). Since the energy transfer in the atmosphere is mainly driven by photons with $h\nu \sim (1 - 10)k_BT$, one can neglect the magnetic effects if $B \ll (m_e c/he)k_BT \sim 10^{10}(T/10^6\,\mathrm{K})$ G. If a substantial fraction of bound atoms or ions is present, the magnetic effects are determined by the ratio $h\nu_B/Z^2\mathrm{Ry} \sim (B/10^9\ \mathrm{G})Z^{-2}$, where Z is a characteristic ion charge, and $\mathrm{Ry} = 13.6$ eV is the Rydberg energy. When this ratio is $\lesssim 1$, magnetic effects on the bound-bound transitions between lower quantum levels, as well as on the bound-free transitions well above photoionization thresholds, can be neglected. Although transitions which involve highly excited levels may be affected by much lower fields, they usually are not important for conditions typical for NS atmospheres.

Thus, depending on atmospheric temperature and chemical composition, one can neglect the magnetic effects on opacities and EOS if $B \ll 10^8 - 10^{10}$ G. This means that there exists at least one class of NSs, millisecond pulsars, for which the magnetic effects can be expected to be small. Four millisecond pulsars have been detected in soft X-rays (Halpern 1996, and references therein). The radiation from at least one of them – a nearby, bright PSR J0437 − 4715, with the field $B \sim 3 \times 10^8$ G – has been shown to have a thermal-like component apparently originating from the NS surface (Becker & Trümper 1993; Edelstein et al. 1995; Halpern et al. 1996). To interpret these data properly, the observed spectra and the light curves should be compared to nonmagnetic atmosphere models. One cannot exclude also that high magnetic fields of ordinary pulsars are concentrated in small "platelets", whereas a substantial fraction of the NS surface has much lower fields (Page et al. 1995). Finally, since the NS magnetic fields are subject to decay (although characteristic time of this decay remains highly uncertain — see, e. g., Bhattachrya 1995), one can expect that very old NSs, most of which do not show pulsar activity, have magnetic fields sufficiently low for nonmagnetic atmosphere models could be applied to analyze their thermal radiation. Detection of two old NS candidates has been reported recently (Stocke et al. 1995; Walter et al. 1996). Although identification of these objects as NSs requires further confirmation, the amount of dead pulsars observable through their thermal radiation should exceed considerably that of active pulsars, so that one can expect more such objects to be discovered in near future.

Thus, investigation of the nonmagnetic NS atmosphere models can be justified not only by their relative simplicity — the models can be applied to analysis of observations of real objects. Although a set of such models has been in R87, there exist several reasons to re-examine the previous results and to continue work on the nonmagnetic models.

(i) New, much improved opacity codes have been developed by the OPAL group, and a comprehensive set of the opacity data has been computed (Iglesias et al. 1992; Rogers & Iglesias 1994). These new opacities substantially exceed those from LAOL for heavy elements just at the densities and temperatures characteristic for the NS atmospheres. Particularly interesting for the application to NS atmospheres is a set of monochromatic opacities for pure iron composition, generated at request of, and in collaboration with, Roger Romani (Romani 1996, private communication). Rajagopal and Romani (1996; hereafter RR96) have used the results to develop modified NS atmosphere models. [1]

(ii) No hydrogen atmosphere models and only three helium models (for $T_{\mathrm{eff}} = 10^{5.5}$, 10^6 and $10^{6.5}$) were presented in R87, and a few hydrogen and helium nonmagnetic models were presented in our previous papers (Shibanov et al. 1992; Zavlin et al. 1994; Pavlov et al. 1995), mainly for comparison with the magnetic models, without a systematic analysis. However, the low-field NSs, including the millisecond pulsars, are assumed to have been passed, during their long life, through an accretion stage when a substantial amount of light elements have been accumulated at the NS surface. (It may even be that the surface magnetic fields are low because of accretion-induced field decay — see, e. g., Bhattacharya 1995). Due to gravitational stratification (Alcock & Illarionov 1980) and/or nuclear spallation reactions which destroy heavy elements (Bildstein et al. 1992, 1993), the upper atmospheric layers can be expected to consist mainly of lightest elements unless they have been dragged downward by convection or burned in nuclear reactions. Only two hydrogen atmosphere models (for $T_{\mathrm{eff}} = 10^{5.5}$ and 10^6 K) were presented in RR96, which is not enough for a detailed analysis of how the atmospheric structure and emergent spectra depend on the model parameters.

[1] We became aware about RR96 after the present paper had been generally completed.

(iii) Only the (local) flux spectra of the emergent radiation have been studied in both R87 and RR96. However, the temperature distribution over the NS surface should be, as a rule, nonuniform due to either the presence of a hot polar cap in active pulsars (which is demonstrated by the light curve of PSR J0437 − 4715 — Becker & Trümper 1993) or anisotropy of the heat conduction in the NS crust (Shibanov & Yakovlev 1996). This means that the flux from a NS is to be determined by integration of the angle-dependent specific intensities over the observable NS surface; this flux may differ substantially from the local flux due to the frequency-dependent limb-darkening effect which has not been investigated for the nonmagnetic models. In addition, gravitational bending of the photon trajectories is to be taken into account to obtain correct light curves of the NS thermal radiation (Shibanov et al. 1995b; Zavlin et al. 1995b, c).

(iv) It would be desirable to verify the models presented in R87 and RR96 using an alternative, more modern numerical approach which has been applied by our group to modeling magnetic NS atmospheres. In particular, that approach takes into account anisotropy of radiation in both solving the radiative transfer and calculating the atmosphere temperature distribution, whereas the Lucy-Unsöld method employed in R87 and RR96 for calculating the temperature distribution is correct only in the case of isotropic radiation field. In addition, Thomson scattering, treated in R87 with an oversimplified approach, and excluded from consideration in RR96, may be important for light element atmospheres at $T_{\rm eff} \gtrsim 10^6$ K and is to be included consistently in the atmosphere modeling.

In this paper we present a set of nonmagnetic NS atmosphere models of different chemical compositions computed with an advanced atmosphere modeling code combined with the OPAL opacities. We study the atmospheric structure, and the spectra and angular distribution of emergent radiation in a wide range of effective temperatures and surface gravities. We consider the atmospheres in radiative equilibrium, which means that the total energy flux is transferred only by radiation, whereas other heat transport mechanisms (convection, electron heat conduction) are of no importance. The models with convection, whichpwhich plays a role at lower $T_{\rm eff}$, will be analyzed elsewhere (see Zavlin et al. 1996 for preliminary results). Our estimates show that, for the models considered, contribution of electron heat conduction to the heat flux never exceeds a few tenths of percent at unit optical depth. It may reach several percent only at very bottoms of heavy element atmospheres with lowest effective temperatures; the intensities of far Wien tails of the emergent radiation formed at these layers are too low to be of any practical importance. It should be mentioned that our estimates of the conductive opacity exceed those of RR96 (making electron heat conduction less important) because RR96 used an approximate equation with the Coulomb logarithm omitted. On the other hand, the equations we use (Hochstim & Massel 1969) also become inaccurate at high densities and low temperatures, so that the problem needs further consideration.

We describe our approach to atmosphere modeling in Section 2, and present the results in Section 3. Some observational implications are discussed in Section 4.

2. General description of the model

2.1. Basic equations

Since a characteristic thickness of the NS atmosphere, $\sim 0.01 - 1$ cm, is much smaller than the NS radius, and characteristic densities are rather high, we consider the plane-parallel atmospheres in local thermodynamic equilibrium. Following a standard approach (e. g., Mihalas 1978), we proceed from the radiative transfer equation in the form of a second-order boundary problem:

$$\mu^2 \frac{\mathrm{d}}{\mathrm{d}y}\frac{1}{k_\nu}\frac{\mathrm{d}}{\mathrm{d}y}u_\nu = k_\nu(u_\nu - S_\nu) \ , \qquad (1)$$

$$\frac{\mu}{k_\nu}\frac{\mathrm{d}}{\mathrm{d}y}u_\nu = u_\nu|_{y=0}, \qquad u_\nu = B_\nu|_{y\to\infty} \ , \qquad (2)$$

where $0 \le \mu \le 1$ is cosine of the angle θ between the normal to the atmosphere and the wave vector, $u_\nu = u_\nu(y,\mu) = \frac{1}{2}(I_\nu^+ + I_\nu^-)$, $I_\nu^+ = I_\nu(y,+\mu)$ and $I_\nu^- = I_\nu(y,-\mu)$ are the specific spectral intensities of the outward- and inward-directed streams of radiation, y is the column density ($\mathrm{d}y = -\rho\,\mathrm{d}z$), and $B_\nu = B_\nu(T(y))$ is the Planck function. The monochromatic opacity $k_\nu = k_\nu(y) = \alpha_\nu(y) + \sigma_\nu(y)$ is the sum of the true absorption opacity α_ν and scattering opacity σ_ν. For the source function $S_\nu = S_\nu(y)$ we use

$$S_\nu = (\sigma_\nu J_\nu + \alpha_\nu B_\nu)k_\nu^{-1} \ , \qquad (3)$$

where $J_\nu = J_\nu(y) = \int_0^1 u_\nu\,\mathrm{d}\mu$ is the mean intensity. This form of the source function implies the isotropic scattering approximation which proved to be very accurate even in the case when scattering dominates over true absorption (e. g., Mihalas 1978). The boundary conditions (2) assume that there is no incident radiation at the outer boundary $y = 0$, and the photon energy density tends to its equilibrium value at large depths.

In the present paper we consider only atmospheres in radiative equilibrium, where convection and electron heat conduction are negligible, and the energy is transferred solely by radiation. In this case the radiative flux is independent of y and coincides with the total flux, $F \equiv \sigma_{SB}\, T_{\rm eff}^4$,

$$\int_0^\infty F_\nu \mathrm{d}\nu = 4\pi \int_0^\infty \mathrm{d}\nu \int_0^1 \mathrm{d}\mu \frac{\mu^2}{k_\nu}\frac{\mathrm{d}u_\nu}{\mathrm{d}y} = \sigma_{SB}\, T_{\rm eff}^4 \ , \qquad (4)$$

where $F_\nu(y)$ is the spectral flux, σ_{SB} is the Stefan-Boltzmann constant, and $T_{\rm eff}$ is the effective temperature.

It follows from Eqs. (1) and (4) that the radiative equilibrium condition can be also presented in the form

$$\int_0^\infty \alpha_\nu (J_\nu - B_\nu) \mathrm{d}\nu = 0 \ . \tag{5}$$

We consider the atmospheres in hydrostatic equilibrium, which implies that the gas pressure is $P = g\, y$, where g is the gravitational acceleration (the radiative force is insignificant for the temperatures of interest, $T_{\rm eff} \ll 10^7$ K). The above equations are to be supplemented with EOS, $P = P(\rho, T)$, and true absorption and scattering opacities, $\alpha_\nu(\rho, T)$ and $\sigma_\nu(\rho, T)$. The opacities can be either extracted from opacity libraries or calculated with the use of atomic data (radiative cross sections). In the latter case, the set of equations of ionization equilibrium (EOIE) should be solved to find the fractions of ions in different stages of ionization as well as the electron number density $N_e(\rho, T)$.

The input parameters of a model are the effective temperature $T_{\rm eff}$, surface gravitational acceleration g (or the NS mass and radius) and chemical composition. Solving these equations yields the atmospheric structure ($T(y)$, $\rho(y)$, $N_e(y)$, etc.), and the radiative field in the atmosphere ($F_\nu(y)$, $J_\nu(y)$, $u_\nu(y,\mu)$, including the angular and spectral distribution of the emergent radiation, $I_\nu(0,\mu) = 2u_\nu(0,\mu)$).

It should be noted that the models give the radiation and the atmospheric structure for a local element of the NS surface. If the surface conditions are not uniform (e. g, the effective temperature may be higher at the magnetic poles), the observable photon flux should be obtained from integration of $I_\nu(0,\mu)$ over the visible NS surface, with allowance for the gravitational redshift and bending of the photon trajectories (e. g., Shibanov et al. 1995b; Zavlin et al. 1995b, c).

2.2. Method of solution

Solving the system of the model equations splits into two parts, each of which can be solved with the knowledge of the other: calculation of the radiation field given the structure of the atmosphere, and calculation the structure given the radiation field. We start from calculating the temperature distribution in the Eddington approximation, integrating the equation

$$\frac{\mathrm{d}}{\mathrm{d}y}\frac{T}{T_{\rm eff}} = \frac{3}{16} k_R \left(\frac{T_{\rm eff}}{T}\right)^3 \tag{6}$$

with the boundary condition $T(0) = 0.841\, T_{\rm eff}$. Here $k_R = k_R(T, \rho)$ is the Rosseland mean opacity which is calculated at each step of the integration, with $\rho(y)$ being found from EOS and hydrostatic equilibrium. The initial atmospheric structure is used to obtain a first approximation for the radiation field.

Computing the radiation field starts from calculating the Eddington factors,

$$f_\nu = J_\nu^{-1} \int_0^1 \mu^2 u_\nu \, \mathrm{d}\mu \quad \text{and} \quad h_\nu = J_\nu^{-1} \int_0^1 \mu u_\nu \, \mathrm{d}\mu \ . \tag{7}$$

In deep layers, where the radiation is nearly isotropic and the diffusion approximation is valid, we have $f_\nu \simeq \frac{1}{3}$ and $h_\nu \simeq \frac{1}{2}$. The dependences of f_ν and h_ν on y account for the depth dependence of anisotropy of radiation. Integrating Eqs. (1) and (2) over μ yields the ordinary differential equation for the mean intensity,

$$\frac{\mathrm{d}}{\mathrm{d}y}\frac{1}{k_\nu}\frac{\mathrm{d}}{\mathrm{d}y} f_\nu J_\nu = \alpha_\nu \, (J_\nu - B_\nu) \ , \tag{8}$$

with the boundary conditions

$$\frac{1}{k_\nu}\frac{\mathrm{d}}{\mathrm{d}y} f_\nu J_\nu = h_\nu J_\nu|_{y=0}, \qquad J_\nu = B_\nu|_{y\to\infty} \ . \tag{9}$$

Now $f_\nu(y)$ and $h_\nu(y)$ can be calculated by solving Eqs. (1), (8) and (7) iteratively: we start from solving Eq. (1) with the source function $S_\nu = B_\nu$ to obtain an initial approximation for f_ν and h_ν from Eq. (7); then we use these f_ν and h_ν to solve (8), substitute the solution J_ν into the source function, and solve Eq. (1) to find new u_ν and, hence, f_ν and h_ν, and so on, until convergence of f_ν and h_ν. Note that at each step of these "inner" iterations we solve ordinary differential equations instead of original integro-differential (with respect to μ and y) Eq. (1).

In principle, one could use $J_\nu(y)$ obtained in the course of the inner iterations to calculate a new atmospheric structure. However, convergence of the "global" iterations can be significantly improved (Auer & Mihalas 1968) if instead we use the solution of the integro-differential (with respect to ν and y) equation

$$\frac{\mathrm{d}}{\mathrm{d}y}\frac{1}{k_\nu}\frac{\mathrm{d}}{\mathrm{d}y} f_\nu J_\nu = \alpha_\nu \, (J_\nu - B_\nu) - \tag{10}$$
$$-\alpha_\nu \frac{\mathrm{d}B_\nu}{\mathrm{d}T} \frac{\int_0^\infty \alpha_{\nu'} (J_{\nu'} - B_{\nu'}) \, \mathrm{d}\nu'}{\int_0^\infty \alpha_{\nu'} (\mathrm{d}B_{\nu'}/\mathrm{d}T) \mathrm{d}\nu'} \ ,$$

with the boundary conditions (9) and with the Eddington factors calculated as described above. Since the spectral flux is

$$F_\nu = \frac{4\pi}{k_\nu}\frac{\mathrm{d}}{\mathrm{d}y} f_\nu J_\nu \ , \tag{11}$$

the additional (as compared to Eq. (8)) integral term in Eq. (10) automatically provides the total radiative flux F to be constant throughout the atmosphere at any given iteration. Moreover, this integral term turns into zero identically when the radiation field and atmospheric structure satisfy the radiative equilibrium condition (5).

The mean intensity found from Eq. (10) is used to calculate a new temperature $T + \delta T$ for each atmospheric layer, with the correction δT equal to the ratio of the two integrals in the additional term in Eq. (10). Once the new $T(y)$ is obtained, we can complete calculation of the atmospheric structure (and new opacities) making use of the hydrostatic equilibrium, EOS and EOIE, and then compute the corresponding radiation field as described above (starting with calculation of the Eddington factors). The global iterations continue until the maximum relative correction $|\delta T/T|$ becomes smaller than a given value (typically $\sim 1\%$). Note that using the modified transfer equation (10) substantially accelerates the global iterations (a reasonable accuracy is reached in 2–4 iterations).

We solve the model equations numerically by discretizing on the depth variable y, photon energy $E = h\nu$ and angular variable μ. Typically, we use a grid with $100-150$ depth points logarithmically spaced between $10^{-8} - 10^{-6}$ and $1 - 10$ g cm^{-2}, $100 - 200$ energy points logarithmically spaced between $0.1\,k_B T_{\rm eff}$ and $60\,k_B T_{\rm eff}$, and 50 angular points for μ between 0 and 1. A fourth-order Hermitian discretization method (Auer 1976) is applied to solve Eqs. (8), (9) and (10). We also use the elimination scheme suggested by Rybicki & Hummer (1991), which provides a higher accuracy in comparison with the standard Gaussian method.

Since the monochromatic opacities of heavy elements (particularly iron) include many thousands of spectral lines, their frequency dependence should be properly binned to use them for construction of the atmosphere models. We average the original monochromatic opacities arithmetically in each bin of the logarithmic frequency grid (typically $(1-2)\times 10^3$ frequency points per bin) and use these binned opacities to compute the atmospheric structure and a "smoothed" spectrum as described above. We checked by varying the number of bins that $\sim 100-200$ bins provide sufficient accuracy (a relative error $\lesssim 1-2\%$) of the atmospheric structure and the total flux. To obtain the spectrum with a fine spectral resolution, we calculate the intensities of the outward- and inward-directed streams,

$$I_\nu^+(y,\mu) = \frac{1}{\mu}\int_y^\infty S_\nu k_\nu \,\exp\left(-\frac{1}{\mu}\int_y^{y_1} k_\nu\,{\rm d}y_2\right)\,{\rm d}y_1 \qquad (12)$$

and

$$I_\nu^-(y,\mu) = \frac{1}{\mu}\int_0^y S_\nu k_\nu \,\exp\left(-\frac{1}{\mu}\int_{y_1}^{y} k_\nu\,{\rm d}y_2\right)\,{\rm d}y_1\ , \qquad (13)$$

with the original monochromatic opacities (at $\sim 10^4$ frequency points). The spectral flux is then computed as

$$F_\nu(y) = 2\pi\int_0^1 \left[I_\nu^+(y,\mu) - I_\nu^-(y,\mu)\right]\mu\,{\rm d}\mu\ . \qquad (14)$$

These "output" spectra can be further smoothed, if needed, with a standard spline procedure.

2.3. Opacities and EOS

The true absorption opacity α_ν is due to the free-free, bound-free and bound-bound transitions; σ_ν is dominated by the Thomson scattering on electrons. The main distinction of the opacities, EOS and EOIE in a NS atmosphere from those in usual stars is due to high non-ideality (pressure effects). For modeling hydrogen/helium atmospheres, we calculate the opacities and EOIE of non-ideal gases using the occupation probability formalism (Hummer & Mihalas 1988) as described by Zavlin et al. (1994). The results of these calculation agree fairly well with the OPAL data (Iglesias et al. 1992) obtained with a quite different approach (Rogers 1986).

For modeling iron atmospheres, we use the opacities and EOS computed by the OPAL group, in collaboration with R. Romani. The opacities k_ν were computed for the domain $\log R = -5\,(1)\,1, \log T = 4.5\,(0.25)\,7.5$ ($R \equiv \rho/T_6^3$, ρ in g cm^{-3}, $T_6 = T/(10^6$ K)). They are provided on a grid of 10^4 photon energies linearly spaced in the range $2\times 10^{-3} k_B T \le E \le 20 k_B T$. To obtain k_ν at given T and ρ, we use the cubic spline interpolation of $\log k_\nu$ with respect to $\log R$ and $\log T$. For $E > 20 k_B T$ we use additional tables for the same R and T and 1 eV $\le E \le 10$ keV.

3. Results

We have computed a set of the atmosphere models for NSs with various effective temperatures $T_{\rm eff}$, gravitational accelerations g and chemical compositions. In this paper we demonstrate representative models for pure hydrogen, helium and iron compositions. The hydrogen and helium models are presented for $\log T_{\rm eff} = 4.7\,(0.3)\,6.5$; higher effective temperatures are not expected to be observed in cooling NSs, and at lower $T_{\rm eff}$ the helium atmospheres become convectively unstable. The iron atmosphere models, where convection can develop at higher $T_{\rm eff}$, are presented for $\log T_{\rm eff} = 5.3\,(0.3)\,6.5$. We chose a "basic" gravitational accelerations $g_{14} \equiv g/(10^{14}$ cm s$^{-2}) = 2.43$ (it corresponds to standard NS mass $M = 1.4 M_\odot$ and radius $R = 10$ km); a few examples are given for $g_{14} = 0.5$ and 4.5.

3.1. Atmospheric structure

The atmospheric structure has not been analized thoroughly in the previous works; however, it is not only interesting in itself — it also allows one to better understand properties of the emergent radiation. Quite different structures of atmospheres composed of light and heavy elements are due to very different opacities. An example of the energy dependence of the opacities at the depths $\log y = -6, -4$ and -2 is shown in Fig. 1 for the hydrogen, helium and iron atmosphere models with $\log T_{\rm eff} = 5.9$, $g_{14} = 2.43$. We see that the Fe opacities, dominated by numerous spectral lines, are, on average, greater than H

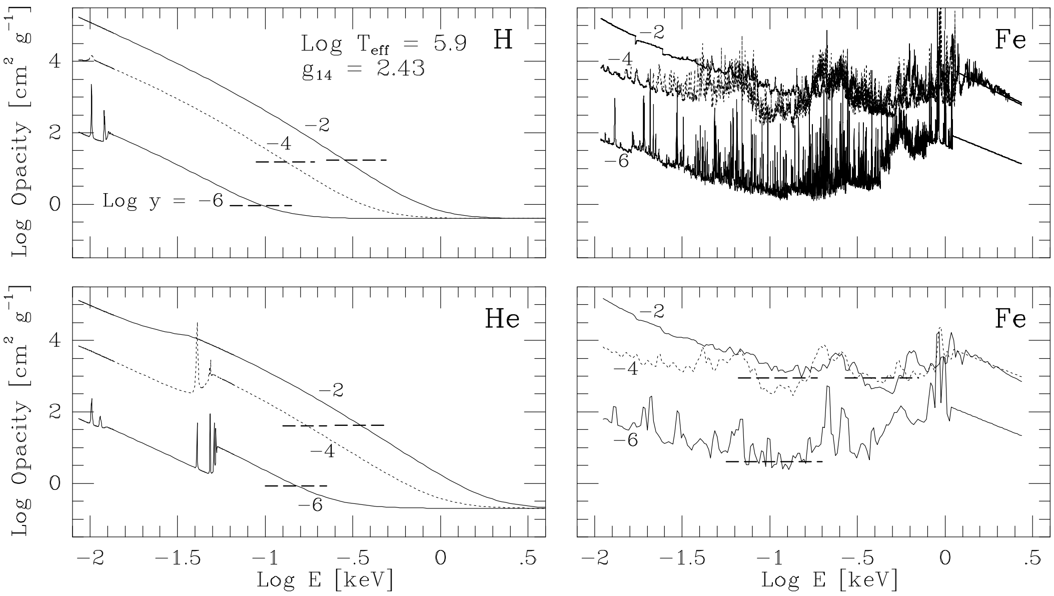

Fig. 1. Monochromatic opacities *vs.* photon energy at the layers $y = 10^{-6}$, 10^{-4} and 10^{-2} g cm^{-2} of the hydrogen, helium and iron atmospheres with $T_{\rm eff} = 10^{5.9}$ K and $g = 2.43 \times 10^{14}$ cm s^{-2}. The upper right panel shows the original Fe opacities (10^4 energy points); the binned opacities (200 points) are shown in the bottom right panel. The horizontal dashed lines demonstrate the Rosseland mean opacities k_R at the corresponding layers.

and He opacities, and their mean slope at the most important frequency range is almost flat. On the contrary, H and He opacities are dominated by the free-free and bound-free transitions ($k_\nu \propto \nu^{-3} \propto E^{-3}$) at moderate and low frequencies (energies), whereas at high frequencies they are dominated by Thomson scattering (independent of ν). These distinctions are responsible for different atmospheric structures and properties of the emergent radiation.

Particularly important component of the atmospheric structure is the depth dependence of temperature, $T(y)$. Examples of $T(y)$ for several values of $T_{\rm eff}$ and for three chemical compositions are demonstrated in Fig. 2. We see that, for any $T_{\rm eff}$, the temperature at a given depth y is systematically higher for iron atmospheres. In other words, a characteristic depth, $y_{\rm eff}$, which can be defined by the equation $T(y_{\rm eff}) = T_{\rm eff}$, is smaller for iron atmospheres ($-4.6 < \log y_{\rm eff} < -2.1$ in our example) than for helium and hydrogen atmospheres ($-3.7 < \log y_{\rm eff} < 0$ and $-2.9 < \log y_{\rm eff} < 0$, respectively, for the same range of $T_{\rm eff}$). Higher temperatures for iron atmospheres at large depths, where $T^4(y) \sim T_{\rm eff}^4 \tau_R = T_{\rm eff}^4 \int_0^y k_R \, {\rm d}y$, are due to higher Rosseland mean opacity k_R (cf. Fig. 1). Substantially higher surface temperatures ($T_s [\equiv T(0)] = (0.78 - 0.81) T_{\rm eff}$ for Fe *vs.* $T_s = (0.31 - 0.53) T_{\rm eff}$ for H, at $\log T_{\rm eff} = 5.3 - 6.5$) can be explained by generally flatter frequency dependence of the Fe opacity, which results in temperature profiles and surface temperatures close to those for the grey atmosphere ($T_s \simeq 0.811 T_{\rm eff}$). The differences between the hydrogen and helium temperature profiles depend on the degree of ionization in the atmosphere, which, in turn, is determined by $T_{\rm eff}$ and g. In particular, at high $T_{\rm eff}$ the light element plasma is completely ionized, and its opacity in deep, dense layers is mainly determined by the free-free transitions: $k_R \sim Z^3 A^{-2} \rho T^{-7/2}$, where Z is the ion charge, and A the atomic weight. Using this expression for k_R, Eq. (6), and EOS for the ideal gas, $\rho \propto A(Z+1)^{-1} g y T^{-1}$, we obtain $T^{15/2} {\rm d}T \propto$

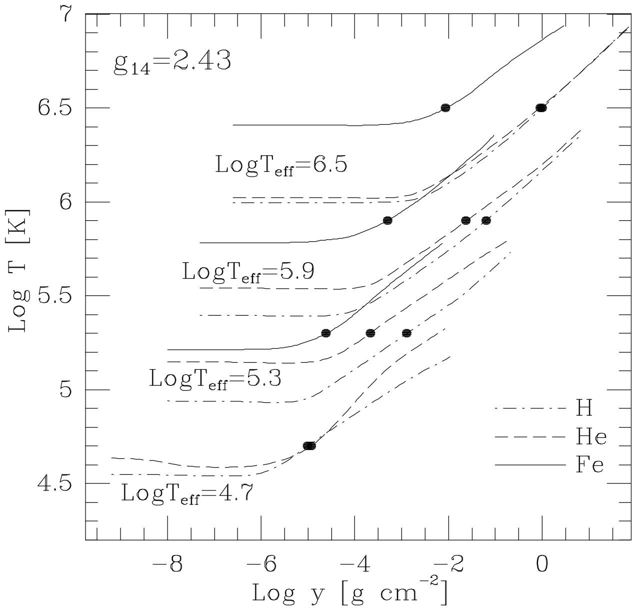

Fig. 2. Temperature profiles $T(y)$ of the models with different effective temperatures and chemical compositions. The filled circles mark the points where $T(y) = T_{\rm eff}$; the corresponding $y = y_{\rm eff}$ can be considered as a characteristic depth of the atmosphere.

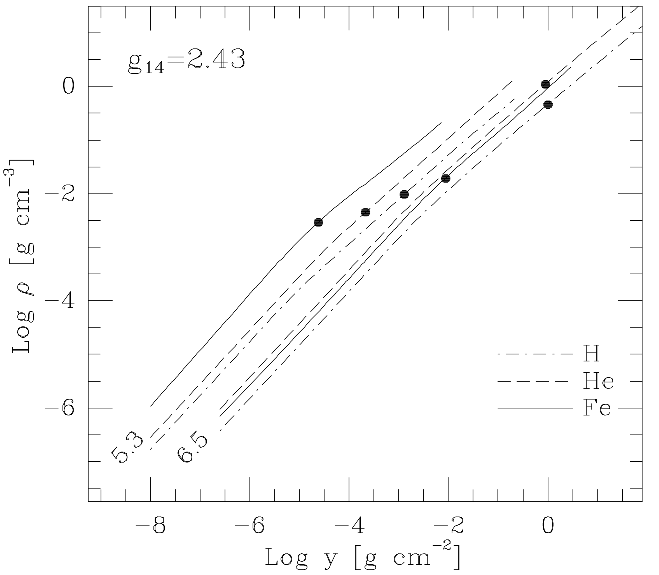

Fig. 3. Mass density profiles $\rho(y)$ for two values of $\log T_{\rm eff}$ = 5.3 and 6.5 and three chemical compositions. The filled circles indicate the characteristic densities $\rho_{\rm eff} = \rho(y_{\rm eff})$ (cf. Fig. 2).

$gZ^3[A(Z+1)]^{-1}y{\rm d}y$, which yields the following equation for the asymptotic behavior of the temperature of a fully ionized atmosphere at large y:

$$T(y) \propto \left(\frac{Z^3}{Z+1}\frac{g}{A}\,T_{\rm eff}^4\right)^{2/17} y^{4/17}\,. \tag{15}$$

The value of the multiplier in front of $y^{4/17}$ for He exceed that for H by 3% only; this means that the temperature profiles are essentially the same at sufficiently large depths, which we observe for the models with $\log T_{\rm eff}$ = 6.5. At $\log T_{\rm eff}$ = 5.9, the hydrogen atmosphere is completely ionized at the most important depths, whereas the helium atmosphere contains a few percent of once-ionized helium, HeII (see Fig. 4), which substantially increases the bound-free opacity (Fig. 1). This leads to a greater difference between the He and H temperatures at $y \sim y_{\rm eff}$. At $\log T_{\rm eff}$ = 5.3 the difference is even more pronounced because a larger fraction of HeII, $\gtrsim 10\%$, is available. Finally, at $\log T_{\rm eff}$ = 4.7, the H atmosphere contains $\sim 10\%$ of neutral atoms HI, and the He atmosphere is mainly composed of HeII, with an admixture of HeI. In both cases opacity is dominated by the bound-free transitions, and the temperature profiles are close to each other at $y \sim y_{\rm eff}$.

The temperature dependence of the He atmosphere with $\log T_{\rm eff}$ = 4.7 shows an interesting anomaly at small y: it slightly increases outward at $\log y \lesssim -7.5$. This inverse behavior is due to substantial growth with y of the HeI fraction at $\log y \lesssim -7$ (see Fig. 4), accompanied by increasing role of the HeI photoionization absorption at $E \gtrsim 20 - 25$ eV. To provide the radiative equilibrium (Eq. (5)) at small y, the local blackbody intensity $B_\nu(T(y))$ is to be greater than the mean intensity $J_\nu(y)$

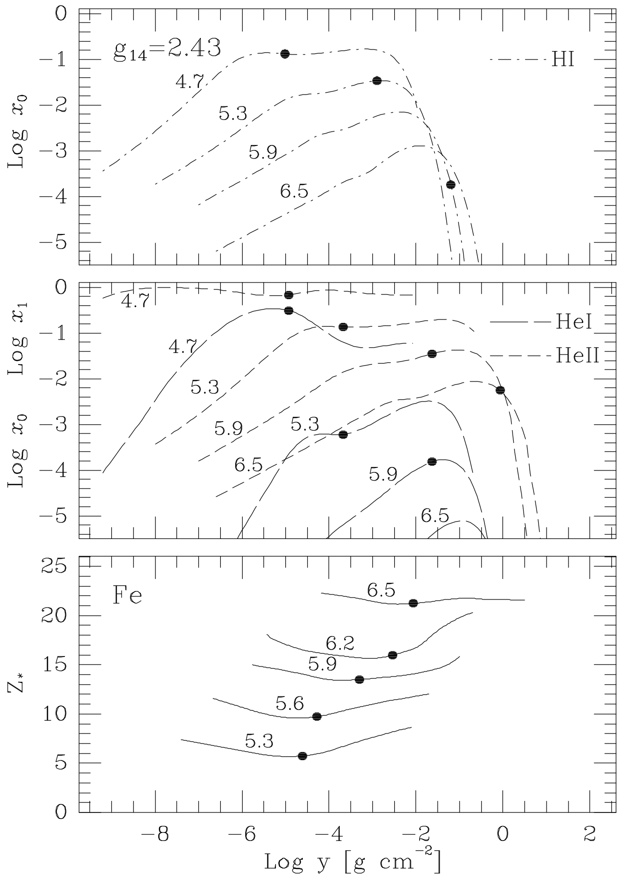

Fig. 4. Depth dependences of ionization for models with different values of $\log T_{\rm eff}$ (numbers near the curves). Two upper panels show profiles of non-ionized hydrogen and helium, $x_0(y)$, and once-ionized helium, $x_1(y)$, for pure hydrogen and helium models. The bottom panel shows the depth dependences of the mean ion charge $Z_*(y)$ for pure iron models. The filled circles show the corresponding quantities at $y = y_{\rm eff}$.

at low energies (below the main photoionization jump), and smaller than $J_\nu(y)$ at high E (above the jump). At $\log y \lesssim -8$ the main jump (provided by HeII) arises at $\simeq 50 - 55$ eV, whereas at $-7 \lesssim \log y \lesssim -6$ the jump is shifted to $\simeq 20 - 25$ eV due to a greater fraction of HeI. Therefore, for energies between approximately $20 - 55$ eV, $B_\nu \gtrsim J_\nu$ at $\log y \lesssim -8$, while the opposite inequality holds at $-7 \lesssim \log y \lesssim -6$. Since J_ν is practically independent of y in all these layers, the Planck function at $\log y \lesssim -8$ should be higher than at $-7 \lesssim \log y \lesssim -6$. This decrease of B_ν at these depths is possible if only the surface temperature $T(0)$ is higher than the temperature in the deeper layers.

Figure 3 shows the depth dependence of the mass density $\rho(y)$ for the models with $\log T_{\rm eff}$ = 5.3 and 6.5. The density grows with y linearly (exponentially with the geometrical depth z) at the upper (exponential) atmosphere, where the temperature is close to T_s. In deep layers, the density grows more gradually due to the steeper temperature growth. The density can be estimated as

$\rho \sim m_H A(Z_* + 1)^{-1} gy(k_B T)^{-1}$, where $Z_* = Z_*(y) = N_e A m_H/\rho$ is the mean ion charge defined as the ratio of the electron number density N_e to the summed number densities of atoms in all stages of ionization. Since the hydrogen and helium atmospheres at the temperatures considered are strongly ionized ($Z_* \simeq Z$), the density of a helium atmosphere at a given y exceeds that of a hydrogen atmosphere with the same $T_{\rm eff}$ and g. In particular, for deep layers of fully ionized atmospheres the curves $\rho(y)$ has a universal slope,

$$\rho \propto Z^{-6/17}(Z+1)^{-15/17}A^{19/17}g^{15/17}T_{\rm eff}^{-8/17}y^{13/17} \qquad (16)$$

so that $\rho^{\rm (He)}(y)/\rho^{\rm (H)}(y) \simeq 2.6$. Iron atmospheres at these temperatures are only partially ionized, and the different disposition of the $\rho^{\rm (Fe)}(y)$ with respect to $\rho^{\rm (He)}(y)$ at $\log T_{\rm eff} = 5.3$ and 6.5 is explained by different degrees of ionization ($Z_* \simeq 5-7$ and $21-22$, respectively — see Fig. 4). Characteristic densities in different models, $\rho_{\rm eff} = \rho(y_{\rm eff})$, are generally lower for iron atmospheres, $\rho_{\rm eff} \sim 0.003 - 0.02$ g cm^{-3}, than for hydrogen/helium atmospheres, $\rho_{\rm eff} \sim 0.005 - 1$ g cm^{-3}, for the range $\log T_{\rm eff} = 5.3 - 6.5$. The ratio $z_{\rm eff} = y_{\rm eff}/\rho_{\rm eff}$ gives a characteristic scale height in an atmosphere; it varies from ~ 0.01 cm for Fe at $\log T_{\rm eff} = 5.3$ to ~ 2 cm for H at $\log T_{\rm eff} = 6.5$.

The atmospheric opacity and, hence, the temperature, density and properties of the emergent radiation depend essentially on the ionization state at different depths. Figure 4 demonstrates the depth profiles of the fractions of ions in different stages of ionization, $x_j = N_j/(N_0 + N_1 + \ldots + N_Z)$ ($j = 0, 1, \ldots, Z$ is the ion charge). We show the nonionized fraction x_0 for the hydrogen models, nonionized and once-ionized fractions, x_0 and x_1, for the helium models, and the mean ion charge $Z_* = \sum_{j=1}^{Z} j x_j$ for the iron models. The hydrogen atmospheres are strongly ionized at the considered temperatures (even at $\log T_{\rm eff} = 4.7$ the nonionized fraction does not exceed 17%); however, the contribution of the bound-free transitions into opacity is not negligible at x_0 as small as $10^{-3} - 10^{-2}$ (cf. Fig. 1). At $\log y \lesssim -2.5$ the values of x_0 are determined by the usual Saha equation: x_0 grows with y at very outer layers, where the temperature is almost constant, due to increasing density; the growth decelerates in deeper layers due to increasing temperature. At large depths, where $\rho \gtrsim 10^{-2} - 10^{-1}$ g cm^{-3}, the fraction x_0 decreases steeply due to pressure ionization. Similar behavior is seen for the helium fractions x_0 and x_1, although the ionization degree is lower than for hydrogen due to higher ionization potentials. At moderate temperatures, the main contribution to the opacity comes from the bound-free transitions of HeII; the non-ionized HeI plays a role at lower $T_{\rm eff}$. The iron atmospheres are only partly ionized even at high $T_{\rm eff}$ and very deep layers (e. .g., Z_* does not exceed $21 - 22$ through the whole atmosphere with $\log T_{\rm eff} = 6.5$) due to very high ionization potentials and binding energies.

The atmospheric structure depends also on the gravitational acceleration g. Our computations show that varying g in the range expected for the surfaces of NSs affects the temperature profile only slightly: $T \propto g^{2/17}$ in very deep layers (see Eq. (15)), and the effect on the surface temperature is even smaller. The characteristic depth and density depend on g much stronger; in particular, $\rho \propto g$ in surface layers, and $\rho \propto g^{15/17}$ in deep layers. The ionization degree is affected accordingly: generally, the ionized fractions grow with g, particularly at the surface layers.

3.2. Spectral flux

In Fig. 5 we show the spectral fluxes of the emergent radiation for selected effective temperatures and three chemical compositions. The blackbody fluxes $\pi B_\nu(T_{\rm eff})$ are also shown for comparison.

We see that the model spectra are substantially different from the blackbody spectra with the same $T_{\rm eff}$. The most striking distinction is much harder high-energy tails of the spectra emergent from H and He atmospheres (see also R87, Pavlov et al. 1995, and RR96). The reason for such behavior is that the H and He free-free and bound-free opacities rapidly decrease with increasing photon energy ($\propto E^{-3}$ in a wide energy range — see Fig. 1), so that the radiation of higher energies is formed in deeper and hotter layers. The maxima of the spectra of strongly ionized atmospheres (at $\log T_{\rm eff} \gtrsim 5.0$ and 5.5 for H and He, respectively) lie at $E = (4.6 - 5.0)k_B T$, i. e., they are shifted by a factor of $1.6 - 1.8$ from the corresponding blackbody maxima towards higher energies. Thomson scattering dominates the opacities at high energies (Fig. 1), which must be taken into account for calculating the high-energy tails (i. e., at $E \gtrsim 1$ keV for the models with $\log T_{\rm eff} = 5.9$).

At lower $T_{\rm eff}$, the light element atmospheres are less ionized, and photoionization edges and spectral lines are seen in their spectra. In particular, the Lyman jump and Lyman-α line of HeII become perceptible in the helium atmosphere spectra at $\log T_{\rm eff} \lesssim 6$, when the fraction of the once-ionized helium is as small as a few percent (see Fig. 4). The same fraction of neutral hydrogen is needed to form the hydrogen Lyman features which become well pronounced at $\log T_{\rm eff} \lesssim 5$.

The low-energy tails ($E \ll k_B T$) of the model spectra follow the Rayleigh-Jeans law ($\propto E^2$) corresponding to the surface temperature $T_s (< T_{\rm eff})$, i. e., $F_\nu/\pi B_\nu = T_s/T_{\rm eff} < 1$. This occurs because the opacities grow with decreasing E so that the low-energy radiation emerges from the very surface layers. The low-energy flux is most strongly suppressed (by a factor of up to $\simeq 3.2$) in hot H and He atmospheres because of smallness of the ratio $T_s/T_{\rm eff}$ (see Fig. 2).

The spectra emitted from the iron atmospheres are much more complicated, mainly due to numerous spectral lines and photoionization edges produced by ions in vari-

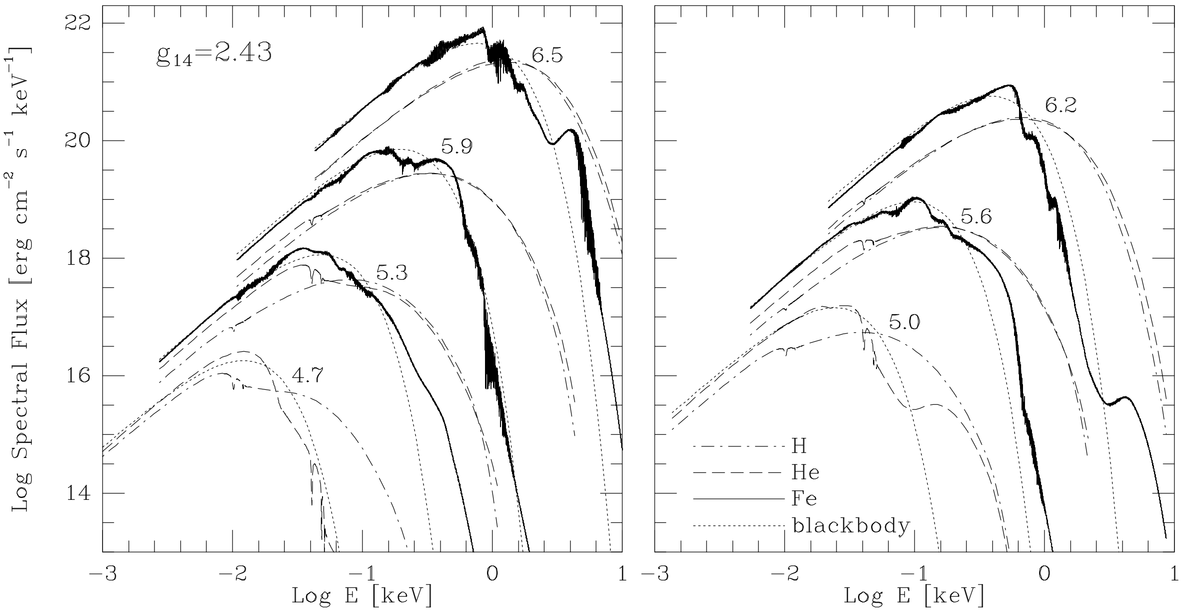

Fig. 5. Spectral fluxes of emergent radiation for hydrogen, helium and iron atmospheres with different values of log $T_{\rm eff}$ (numbers near the curves). Dotted curves show the corresponding blackbody fluxes $\pi B_\nu(T_{\rm eff})$.

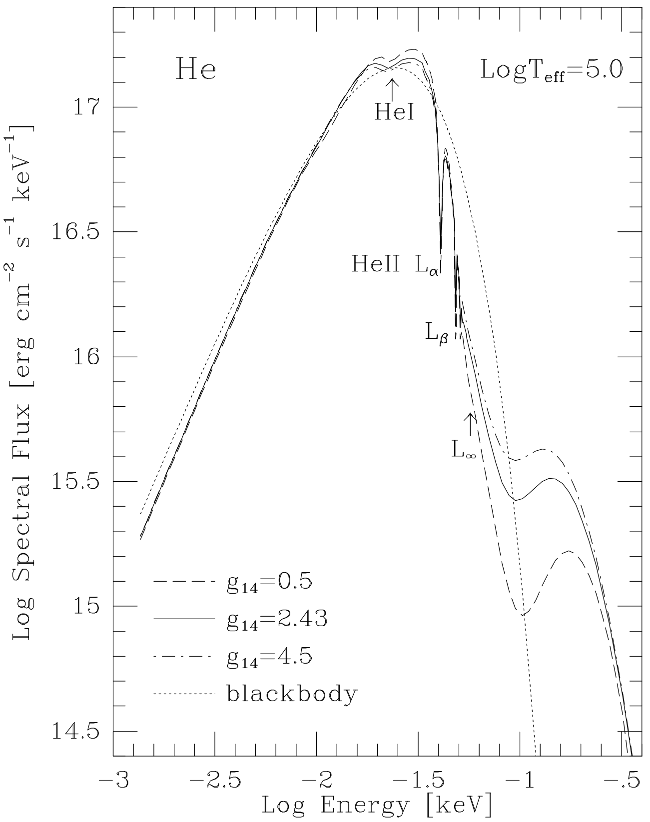

Fig. 6. Spectral fluxes emergent from helium atmospheres with $T_{\rm eff} = 10^5$ K and different surface gravities $g = g_{14} \times 10^{14}$ cm s^{-2}: $g_{14} = 0.5$ (dashed curve), $g_{14} = 2.43$ (solid) and $g_{14} = 4.5$ (dot-dashed).

ous stages of ionization. Generally, they are closer to the blackbody spectra, and their high-energy tails are, on average, softer than those emitted from light element atmospheres; their low-energy tails lie only slightly below the blackbody (Rayleigh-Jeans) spectra. The reason is that the energy dependence of the iron opacities, in spite of its complexity, is, on average, flatter than that for H and He. This makes the emergent spectrum to be closer to the grey atmosphere spectrum which, in turn, only slightly differs from the blackbody spectrum. However, the local deviations from the blackbody spectra are quite substantial, especially in the regions of the photoionization edges, and strongly dependent on the effective temperature.

Figure 6 demonstrates how the gravitational acceleration affects the spectral flux emitted by the helium atmosphere with log $T_{\rm eff} = 5.0$. The effect is seen most vividly in the Lyman continuum of HeII ($E > 54$ eV): the Lyman discontinuity becomes progressively smoothed, and the trough at $E \sim 0.1$ keV becomes shallower, with increasing g. This occurs because the density grows with g and the pressure effects smooth out the photoionization jump in the opacity spectra (Zavlin et al. 1994). The gravity effect (pressure broadening) is also seen in the profiles of the absorption lines, particularly of the 20 eV line of HeI. At higher temperatures, when the light element atmospheres are strongly ionized and the spectra are continuous, the gravity effect becomes insignificant. In the case of iron composition the effect of surface gravity can be seen at higher temperatures.

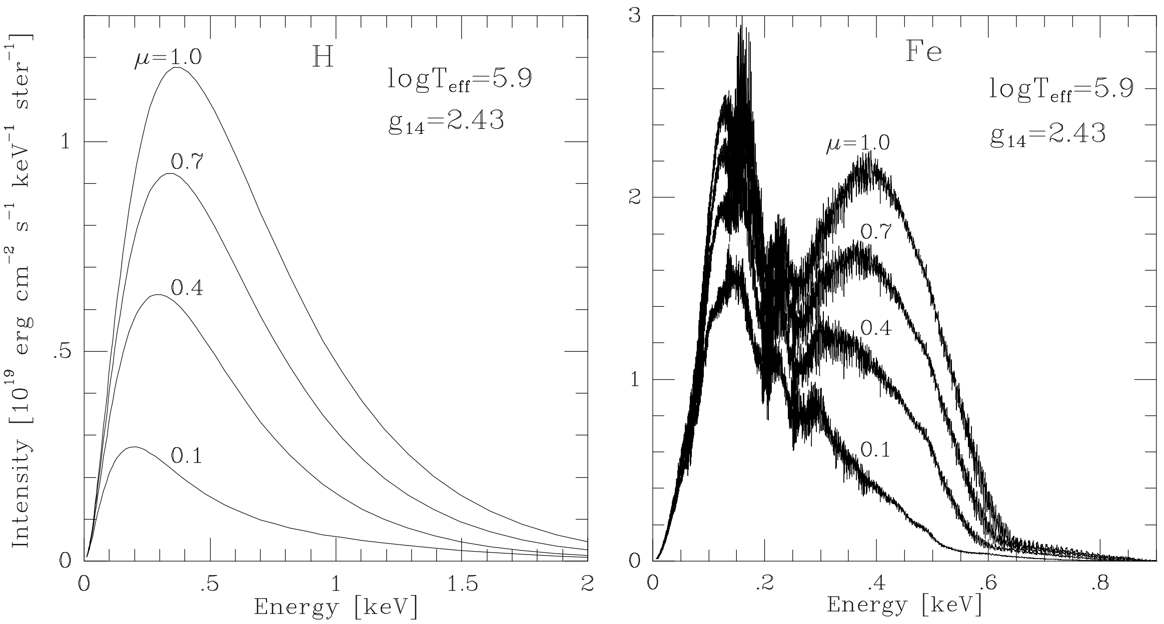

Fig. 7. Spectra of the specific intensity of emergent radiation for the hydrogen and iron atmospheres with $T_{\rm eff} = 10^{5.9}$ K at different values of $\mu = \cos\theta$ (numbers near the curves); θ is the angle between the surface normal and direction of emission.

3.3. Specific intensities: spectra and angular distributions

Figure 7 demonstrates spectra of the specific intensities of the emergent radiation at different angles $\theta = \arccos\mu$ between the direction of emission and the surface normal for the models with hydrogen and iron compositions and the effective temperature of $10^{5.9}$ K. We see that the intensity is rather anisotropic — it decreases with increasing θ (limb-darkening effect). This is explained by the fact that radiation emitted at larger θ escapes from shallower atmospheric layers where the temperature is lower. The anisotropy depends on photon energy (the intensity spectrum varies with θ) and on chemical composition of the atmosphere. Note that the maximum of the intensity spectrum shifts towards lower energies with increasing θ.

The energy-dependent degree of anisotropy can be described by the ratio

$$a_\nu = \frac{I_\nu(\mu = 1) - I_\nu(\mu = 0)}{I_\nu(\mu = 1) + I_\nu(\mu = 0)} \qquad (17)$$

plotted in Fig. 8; it varies from 0 to 1 for atmospheres with the temperature growing inward monotonously. For the light element atmospheres, the anisotropy is small at low energies because the radiation emerges from surface layers at any θ. It grows with E because radiation escapes from hotter layers at $\theta = 0$. At very large E, when opacity is dominated by Thomson scattering, the angular dependence of the intensity is determined by the Ambartsumian-Chandrasekhar function $H(\mu)$ (e. g., Chandrasekhar 1960), and the degree of anisotropy is $a_\nu = 0.488$ (qualitatively, one can use the diffusion approximation, which yields $I_\nu(\mu) \propto 1{+}1.5\mu$ and $a_\nu \simeq 0.43$).

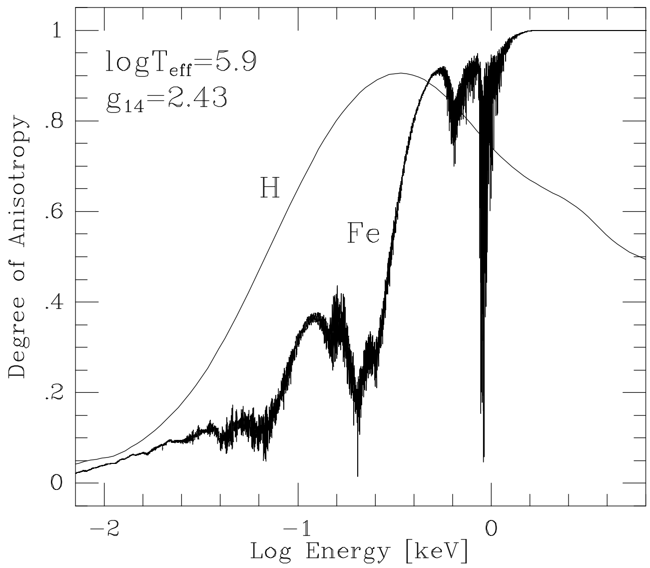

Fig. 8. Degree of anisotropy a_ν (Eq. (17)) *vs.* photon energy for radiation emergent from hydrogen and iron atmospheres with the same parameters as in Fig. 7.

In the case of iron atmospheres, the anisotropy is quite different. In particular, it is very small in the regions of strong spectral lines (e. g., around 0.2 and 1 keV) which originate from the surface layers. (Similar reduction of anisotropy near the spectral lines takes place for the light element atmospheres at lower $T_{\rm eff}$.) The radiation from the iron atmospheres is very anisotropic ($a_\nu \to 1$) at high energies because the opacity keeps decreasing with increasing E (Thomson scattering is negligible — see Fig. 1).

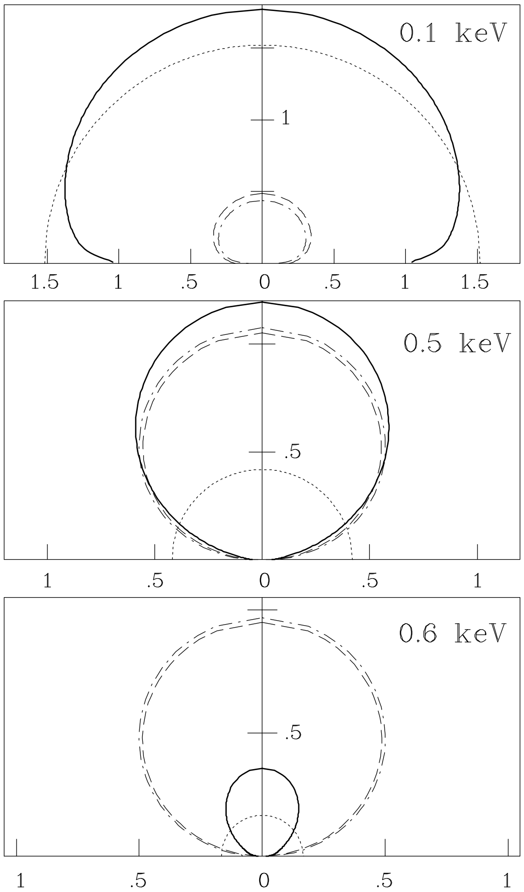

Fig. 9. Polar diagrams of the specific spectral intensities (in units of 10^{19} erg cm^{-2} s^{-1} keV^{-1} ster^{-1}) emitted from hydrogen, helium and iron atmospheres (dash-dotted, dashed and solid lines, respectively) with $T_{\rm eff} = 10^{5.9}$ K, $g = 2.43 \times 10^{14}$ cm s^{-2} at three values of photon energy depicted at the upper-right corners of the panels. The atmosphere normal is directed upward. The dotted lines show the corresponding (isotropic) blackbody intensities.

Figure 9 shows representative angular distributions of the specific intensity emergent from hydrogen, helium and iron atmospheres at different photon energies. Althoug these distributions do not show the prominent features characteristic of radiation emitted from strongly magnetized NS atmospheres (see Fig. 4 in Shibanov & Zavlin 1995), this picture clearly illustrates strong dependences of the distributions on both the energy and chemical composition.

4. Discussion

The presented examples of the atmosphere models show that the atmospheric structure and the properties of emergent radiation depend substantially on the chemical composition of radiating layers and on the value of the effective temperature $T_{\rm eff}$. For the light element atmospheres with a relatively high effective temperatures ($\log T_{\rm eff} \gtrsim 5.3$ for hydrogen, $\log T_{\rm eff} \gtrsim 6$ for helium), the atmospheric matter is strongly ionized, the (continuous) spectrum is much harder at X-ray energies than the blackbody spectrum, and the flux is lower than the blackbody flux at low (UV/optical) energies. For lower $T_{\rm eff}$, spectral features arise in the emergent spectra, particularly in the UV/EUV domain. These distinctions mean that fitting thermal spectra observed from NSs with a blackbody model may be quite misleading. In particular, the blackbody fit of the *high-energy* (X-ray) tail of an observed spectrum would yield systematically *overestimated effective temperature* and *underestimated A/d^2 ratio* (A is the area of the radiating surface, and d is the distance). The error introduced depends on the energy range and response function of the specific detector; e. g., for the *ROSAT* PSPC the temperature may be overestimated by a factor of up to $\simeq 3$, and A/d^2 underestimated by more than an order of magnitude, at detectable NS temperatures. On the contrary, *at low* (UV-optical) *energies* $T_{\rm eff}$ is *underestimated* or *A/d^2 overestimated*, typically by a factor of $2-3$. To obtain reliable estimates of these quantities, one should fit the results with various model atmosphere spectra. It may happen that several models (e. g., with different chemical compositions) would equally well fit the data in a narrow spectral range. To avoid the ambiguity, multiwavelength (e. g., optical through X-ray) observations should be carried out, whenever possible, and fitted with the atmosphere models.

Spectra of heavy element atmospheres are much more complicated — mainly because of numerous spectral lines, as we see from the examples of iron atmospheres. Note that although the shapes of our model spectra are qualitatively similar to those obtained in RR96, the quantitative differences are significant, especially in domains around the strong photoionization features. The difference may arise from both the different procedures for opacity binning and different numerical approaches used for the modeling (e. g., due to the inaccuracy of the Lucy-Unsöld temperature correction procedure used in RR96). Although the overall shape of the iron atmosphere spectra is not so drastically different from the blackbody, using blackbody models for fitting in narrow energy intervals may be even more misleading than for light element atmospheres because even the smoothed shape of the atmosphere spectrum depends very sharply on $T_{\rm eff}$. For instance, we see from Fig. 5 that increasing $T_{\rm eff}$ by a factor of 2 completely changes the shape of the iron atmosphere spectrum, and fitting the spectra with the blackbody in a range of, e. g., $0.2-0.6$ keV would lead to quite different (and quite irrelevant) results.

We do not know a priori what is the chemical composition of the NS surfaces. We can only expect that if there are light elements, they should concentrate at the very surface, but we cannot exclude that the light elements are virtually absent, and the surface layers are composed of heavier elements. To investigate the chemical composition, observations with higher spectral resolution in the soft X-ray range would be very useful. Our examples of the iron models show that the main spectral features (groups of lines and/or photoionization edges) can be resolved with a quite moderate resolution, $\sim 3-30$, which can be easily achieved with modern CCD detectors. Thus, soft X-ray observations of NSs with future missions (*AXAF*, *XMM*, *ASTRO-E*) and their interpretation with the NS atmosphere models will be able to determine directly which elements reside at the NS surface.

Our results also show a very important property of the atmospheric radiation — it is anisotropic, with anisotropy depending on frequency. This dependence is different for different chemical compositions and effective temperatures. This means that if the temperature is not uniform over the NS surface (which is very plausible for real NSs), one not only should take the anisotropy into account to explain the light curves, but also one cannot fit properly the spectra without allowance for anisotropy. To calculate the flux as measured by a distant observer, one should integrate the specific fluxes, $I_\nu \cos\theta$, over the visible NS surface with allowance for the gravitational redshift and bending the photon trajectories. For instance, if the radiation originates from a small hot spot (polar cap) with a uniform $T_{\rm eff}$ and chemical composition, the flux as measured by a distant observer is given by the equation (Zavlin et al. 1995c)

$$F_\nu^{\rm obs} = \frac{A_a}{d^2}\,\frac{1}{(1+z)^3}\,I_{\nu_0}(\mu_c)\ , \qquad (18)$$

where A_a is the apparent area of the hot spot, $z = [1-(2GM/c^2R)]^{-1/2} - 1$ is the gravitational redshift, $\nu_0 = (1+z)\nu$, μ_c is the cosine of the angle θ_c between the radius-vector of the spot center and wave vector of the photon which travels to the observer along the bended trajectory. For realistic NS radii, $R \gtrsim 5.6(M/M_\odot)$ km ($z \lesssim 0.45$), the apparent area can be estimated as $A_a \simeq \pi R^2\gamma^2\mu_c$, where γ is the angular size of the spot. The important feature of Eq. (18) is that the observed flux is proportional not to the local flux, but to the specific intensity whose spectrum (see Figs. 5 and 7) is substantially different from that of the redshifted local flux used in RR96 (their Eq. (7)).

The low-field atmosphere models can be directly applied to the nearby ($d \sim 140$ pc) millisecond pulsar PSR J0437 − 4715 ($P = 5.75$ ms) detected with the *ROSAT* PSPC (Becker & Trümper 1993) and *EUVE* DS (Edelstein et al. 1995; Halpern et al. 1996). Fitting the *ROSAT* spectrum of this low-field ($B \sim 3\times10^8$ G) pulsar with the single-component blackbody model proved to be unsatisfactory — the best-fit blackbody flux (corresponding to $T = 1.5\times10^6$ K) is lower than the observed flux in high-energy PSPC channels (above $\simeq 1$ keV). However, the *ROSAT* spectrum can be satisfactorily fitted with double-component models. For the "power-law + blackbody" fit, Becker & Trümper (1993) obtained $T = 1.7\times10^6$ K and the radiating area $A = 0.05$ km^2, while Halpern et al. (1996) obtained $T = (1.0-3.3)\times10^6$ K and $A = 0.008-1.1$ km^2. In this model, the power law spectrum is of a nonthermal origin, whereas the blackbody spectrum is produced by the hot polar cap of the pulsar. It remains unclear with this interpretation why there is no a phase shift between the pulsations at low energies (power law component) and high energies (thermal component) — being generated at different distances from the NS surface, these components are expected to be phase-shifted and to have different shapes. The values of the emitting area are also uncomfortably low in comparison with that expected from standard models for the radio pulsar polar cap, $A = 2\pi^2R^3/(cP) \sim 10$ km^2 (Arons 1981). Edelstein et al. (1995) ruled out that this two-component fit is compatible with the *EUVE* data, whereas Halpern et al. (1996) came to the opposite conclusion and explained the *EUVE* flux with the power law component.

It is natural to expect that fitting of the same data with the model atmosphere spectra and light curves would yield quite different results. Indeed, our preliminary analysis of both the *ROSAT* and *EUVE* data indicates that a single-component model, in which the soft X-ray radiation originates from two polar caps of areas $A \simeq 2-3$ km^2 covered with hydrogen or helium with $T_{\rm eff} \simeq (0.9-1.0)\times10^6$ K, fits satisfactorily both the spectra and the light curves (Becker et al. 1996). These results differ substantially from those of RR96 who fitted the J0437-4715 spectrum with the local flux spectra, without allowance for the limb darkening and gravitational lensing. It worths noting that the atmosphere models can be used to predict the flux from the NS in the far-UV range ($\lambda \lesssim 2000-3000$ Å), where it should overtake the flux of the cold ($T \simeq 4000$ K) white dwarf companion. Measuring this flux (e. g., with *HST*) would be a critical test to distinguish between different models of the radiating region. Another important test of the models would be to observe the pulsar radiation in the soft X-ray range with a spectral resolution sufficient to resolve spectral features; observations at moderate X-ray energies ($\sim 1-10$ keV) would be useful to constrain the power law component. Such observations would be quite feasible with future X-ray missions (*SAX*, *AXAF*, *XMM*, *ASTRO-E*).

Acknowledgements. We thank F. J. Rogers and C. A. Iglesias for providing the OPAL library data, J. Trümper for stimulating discussions. We are grateful to the referee, R. W. Romani, whose remarks helped us to improve this paper. This work was partly supported by RFFI grant RBRF 96-02-16870A, INTAS grant 94-3834 and NASA grant NAG5-2807. V. E. Zavlin acknowledges the Max-Planck fellowship.

References

Alcock C., Illarionov A. F., 1980, ApJ, 235, 534
Arons J., 1981, ApJ, 248, 1099
Auer L. H., 1976, JQSRT, 16, 931
Auer L. H., Mihalas, D., 1968, ApJ, 151, 311
Becker W., Trümper, J., 1993, Nat., 365, 528

Becker W., Trümper, J., Pavlov, G. G., Zavlin, V. E., 1996 (in preparation)
Bhattacharya D., 1995, in: Alpar M. A., Kiziloğlu Ü., van Paradijs J. (eds). The Lives of the Neutron Stars. Kluwer, Dordrecht, p. 153
Bildstein L., Salpeter E. E., Wasserman I., 1992, ApJ, 384, 143
Bildstein L., Salpeter E. E., Wasserman, I., 1993, ApJ, 406, 615
Chandrasekhar S., 1960, Radiative Transfer. Dover Publications, New York
Edelstein J., Foster R. S., Bowyer, S., 1995, ApJ, 454, 442
Foster, R. S., Edelstein, J., Bowyer, S., 1996, in Bowyer S. and Malina R, (eds.), Proc. IAU Colloq. 152. Kluwer, Dordrecht, p. 437
Halpern J. P., 1996, ApJ, 459, L9
Halpern J. P., Martin C., Marshall H. L., 1996, ApJ (in press)
Hochstim, A. R., and Massel, G. A., 1969, in: Hochstim, A. R. (ed.). Kinetic processes in Gases and Plasmas. Academic Press, New York, p. 142
Hummer D. G., Mihalas D., 1988, ApJ, 331, 794
Iglesias C. A., Rogers F. J., Wilson B. G., 1992, ApJ, 397, 717
Kaminker A. D., Pavlov G. G., Shibanov Yu. A., 1983, Ap&SS, 86, 249
Mihalas D., 1978, Stellar Atmospheres. Freeman, San Francisco
Miller M. C., 1992, MNRAS, 255, 109
Ögelman H., 1995, in: Alpar M. A., Kiziloğlu Ü., van Paradijs J. (eds). The Lives of the Neutron Stars. Kluwer, Dordrecht, p. 101
Page D., Shibanov Yu. A., Zavlin, V. E., 1995, ApJ, 451, L21
Pavlov G. G., Shibanov Yu. A., Ventura J., Zavlin, V. E., 1994, A&A, 289, 837
Pavlov G. G., Shibanov Yu. A., Zavlin V. E., Meyer R. D. 1995, in: Alpar M. A., Kiziloğlu Ü., van Paradijs J. (eds). The Lives of the Neutron Stars. Kluwer, Dordrecht, p. 71
Pavlov G. G., Stringfellow G. S., Córdova, F. A., 1996, ApJ (in press)
Pethick C. J., 1992, Rev. Mod. Phys., 64, 1133
Rajagopal M., Romani R. W. (RR96), 1996, ApJ (in press)
Rogers F. J., 1986, ApJ, 310, 723
Rogers F. J., Iglesias C. A., 1994, Science, 263, 50
Romani R. W. (R87), 1987, ApJ, 313, 718
Rybicki G. B., Hummer D. G., 1991, A&A, 245, 171
Shibanov Yu. A., Yakovlev D. G., 1996, A&A (in press)
Shibanov Yu. A., Zavlin V. E., 1995, Astron. Let., 21, 3
Shibanov Yu. A., Zavlin V. E., Pavlov G. G., Ventura J., 1992, A&A, 266, 313
Shibanov Yu. A., Zavlin V. E., Pavlov G. G., Ventura J., Potekhin, A. Yu., 1993, in: Van Riper K. A., Epstein R. I., Ho C. (eds). Isolated Pulsars. Cambridge Univ. Press, Cambridge, p. 174
Shibanov Yu. A., Zavlin V. E., Pavlov G. G., Ventura J., 1995a, in: Alpar M. A., Kiziloğlu Ü., van Paradijs J. (eds). The Lives of the Neutron Stars. Kluwer, Dordrecht, p. 91
Shibanov Yu. A., Pavlov G. G., Zavlin V. E., Qin L., Tsuruta S., 1995b, in: Böhringer H., Morfill G. E., Trümper J. (eds). 17th Texas Symposium on Relativistic Astrophysics. Annals of New York Academy of Science 759, p. 291
Stocke J. T., Wang Q. D., Perlman E. S., Donahue M. E., Schachter J. F., 1995, AJ, 109, 1199
Tsuruta, S., 1995, in: Alpar M. A., Kiziloğlu Ü., van Paradijs J. (eds). The Lives of the Neutron Stars. Kluwer, Dordrecht, p. 133
Ventura J., Shibanov Yu. A., Zavlin V. E., Pavlov G. G., 1993, in: Van Riper K. A., Epstein R. I., Ho C. (eds). Isolated Pulsars. Cambridge Univ. Press, Cambridge, p. 168
Walter F. M., Wolk S. J., Nuehäuser R., 1996, Nature, 379, 233
Zavlin V. E., Pavlov G. G., Shibanov Yu. A., 1994, Astron. Astrophys. Transact., 4, 307
Zavlin V. E., Pavlov G. G., Shibanov Yu. A., Ventura J., 1995a, A&A, 297, 441
Zavlin V. E., Pavlov G. G., Shibanov Yu. A., 1995b, in: Voges W., Wiedenmann G., Morfill G. E., Trümper J. (eds). 17th Texas Symposium on Relativistic Astrophysics. MPE Repot 261, p. 49
Zavlin V. E., Shibanov Yu. A., Pavlov G. G., 1995c, Astron. Let., 21, 149
Zavlin V. E., Pavlov G. G., Shibanov Yu. A., Rogers F. J., and Iglesias C. A., 1996, in: Zimmermann H.-U., Trümper J., Yorke H. (eds). Röntgenstrahlung from the Universe. MPE Report 263, p. 209

This article was processed by the author using Springer-Verlag LaTeX A&A style file *L-AA* version 3.